*Journal of The Electrochemical Society*, **166** (4) A507-A514 (2019)
0013-4651/2019/166(4)/A507/8/$38.00 © The Electrochemical Society


# Cation Molecular Structure Affects Mobility and Transport of Electrolytes in Porous Carbons

**Naresh C. Osti,[1,z] Boris Dyatkin,[2,a] Alejandro Gallegos,[3] David Voneshen,[4] Jong K. Keum,[1] Ken Littrell,[1] Pengfei Zhang,[5] Sheng Dai,[5,*] Jianzhong Wu,[3] Yury Gogotsi,[2,*] and Eugene Mamontov[1,z]**

[1]*Neutron Scattering Division, Oak Ridge National Laboratory, Oak Ridge, Tennessee 37831, USA*
[2]*Department of Materials Science and Engineering and A. J. Drexel Nanomaterials Institute, Drexel University, Philadelphia, Pennsylvania 19104, USA*
[3]*Department of Chemical and Environmental Engineering, University of California–Riverside, Riverside, California 92521, USA*
[4]*ISIS Pulsed Neutron and Muon Source, STFC Rutherford Appleton Laboratory, Harwell Campus, Didcot, Oxfordshire OX11 0QX, United Kingdom*
[5]*Chemical Science Division, Oak Ridge National Laboratory, Oak Ridge, Tennessee 37831, USA*

We examined the electrosorption and ion dynamics of imidazolium-based room temperature ionic liquids (RTILs) having short (3-carbon, $C3mim^+$) and long (12-carbon, $C12mim^+$) cations, that is, 1-propyl-3-methylimidazolium bis(trifluoromethylsulfonyl)imide (C3mimTFSI) and 1-dodecyl-3-methylimidazolium bis(trifluoromethylsulfonyl)imide (C12mimTFSI), confined in ordered mesoporous carbon (OMC) and analyzed the influence of the cation alkyl chain length on the ion dynamics and the capacitive behavior using electrochemical measurements together with quasi-elastic neutron scattering (QENS) observations and classical density functional theory (cDFT) computations. Electrochemical tests highlighted the significant influence of specific applied potentials on accumulated charge storage densities and on the limits of saturation of larger electrolytes in the pores. Computational analyses corroborated these findings and predicted a 16% increase in the capacitance of the smaller-cation electrolyte under high applied potentials. However, QENS experiments revealed a behavior of decoupling of alkyl chain dynamics from the ring in electrolytes with larger ions. cDFT calculations identified density spikes for $C12mim^+$ away from the pore walls to further corroborate this unique behavior. Our insights into chain length-dependent dynamics and electrosorption in complex electrolyte-electrode systems deepen fundamental understanding of confined RTIL electrolyte behavior in the porous carbon electrodes.
 [DOI: 10.1149/2.0131904jes]

Manuscript submitted November 29, 2018; revised manuscript received January 18, 2019. Published February 13, 2019.

Solvent-free (neat) electrolytes offer significant advantages in electrochemical energy harvesting, conversion, and storage applications.[1,2] These systems increase electrolyte stability across a wide range of temperatures and electric potentials, minimizing irreversible decomposition and breakdown of electrolyte.[3,4] Room temperature ionic liquids (RTILs) are poorly coordinated organic salts that dissociate into ions without the need for a solvent, serve as electrolytes in RTIL-based supercapacitors. These systems are non-volatile, non-flammable, and much more electrochemically stable than conventional aqueous or organic electrolyte alternatives.[5,6] Intuitively, resulting ion behaviors in pores are substantially different from traditional electric double layer (EDL) paradigms and, subsequently, are contingent on the ionic properties, their electrosorption dynamics, and interactions with electrode surfaces.[7]

In order for supercapacitors to efficiently charge and discharge, the electrode and electrolyte components require concomitant tuning and optimization. Intrinsic properties of both electrodes (pore architecture, surface chemistry) and electrolytes (ion dimensions, chemical composition) influence the overall device capacitance and rate handling.[8–10] In order to meet the demands for electrolytes that offer exceptional performance at high voltages (especially negligible vapor pressure, high ionic conductivity, and thermal stability), prior research efforts have yielded a broad variety of viable ionic liquids.[11–13] With respect to the electrode component, numerous porous materials[9,10,14] have been tailored in order to match corresponding electrolytes and maximize charge storage and capacitance. A critical parameter that governs the electrochemical performance of EDLCs remains the quantity of accessible electrode pore surface on which ions can be electro-adsorbed. Carbon materials with internal surfaces[15] offer over 2,000 $m^2\ g^{-1}$ of available electrode surface area for ion accumulation.[16,17] However, important trade-offs between narrower pores (which densely pack ions) and wider pores (which allow efficient ion mobilities) are required for optimal electrode systems.[18–21] Consequently, careful analysis of essential properties of electrodes and electrolytes and balancing of desired attributes is required in order to maximize their performance capabilities of supercapacitors.

In order to assess essential fundamental behaviors that govern the performance of supercapacitors, we investigated electrodynamic and electrochemical performance of two RTILs, 1-propyl-3-methylimidazolium bis(trifluoromethylsulfonyl)imide (C3mimTFSI) and 1-dodecyl-3-methylimidazolium bis(trifluoromethylsulfonyl)imide (C12mimTFSI), that incorporate identical imidazolium rings and anions that possess different alkyl chain lengths on each of their respective cations. Subsequently, such divergently sized electrolytes differ greatly in their ability to enter narrow pores, arrange in co-ion and counterion layers on charged surfaces, and shuffle past each other during dynamic potential conditions. We confined these electrolytes in ordered mesoporous carbon (OMC) that included both micropores and mesopores and, therefore, allowed insight into both tightly confined and relatively unrestricted electrolyte dynamics. We complemented empirical electrochemical measurements (in potentiodynamic conditions) and neutron scattering observations (in electrochemically neutral conditions) with computational analysis (classical density functional theory) in order to provide theoretical explanations. Electrochemical results highlighted the significance of the cation size on impedance and rate handling capabilities, while charge storage capacities further suggested a voltage-dependent saturation limit for the larger electrolyte species. When we increased the cation alkyl chain length from 3 to 12, we noted a corresponding 16% capacitance decrease at high voltages. While electrochemical measurements involved intrinsic co-linked electrosorption of cations and anions, quasi-elastic neutron scattering (QENS) measurements focused on the cations. In particular, they revealed decoupling of the alkyl chain dynamics from the motions of the imidazolium ring that occurred in cations with larger alkyl chains. Our approach offers important insights into behaviors of charge carriers during electrosorption and, in place of dated conventional concepts, offers foundations for more accurate electric double layer models.

*Electrochemical Society Member.
[a]Present address: U.S. Naval Research Laboratory, Washington, DC 20375, USA.
[z]E-mail: ostinc@ornl.gov; mamontove@ornl.gov

## Experimental

***Porosimetry.***—A Quadrasorb (Quantachrome Instruments, Boynton Beach, FL) Gas Sorption Analyzer was used to collect information regarding the specific surface area (SSA) and pore size distribution (PSD) of the original ordered mesoporous carbon (OMC) material. The OMC was synthesized following the established procedure.[22] The instrument collected isothermal measurements at 77 K (liquid $N_2$ coolant) with a nitrogen adsorbate in the 0.0075–0.995 $P/P_0$ relative pressure regime. The SSA was calculated using the Brunauer-Emmett-Teller (BET) equation for adsorption values collected in the 0.05–0.30 $P/P_0$ range.[23] The PSD was derived using Quenched Solid Density Functional Theory (QSDFT) analysis of the adsorption branch.[24] Quadrawin Software (Quantachrome Instruments) was used for all calculations. Ion dimensions were approximated from calculations of molecular models of the electrolyte species produced using the Molinspiration Cheminformatics 2018 software package (http://www.molinspiration.com).

***Electrochemistry measurements.***—Electrodes were prepared according to previously developed procedures.[25,26] OMC particles were dispersed in ethanol and mixed together with a polytetrafluoroethylene (PTFE) polymer binder in a 95:5 w/w ratio of carbon to polymer. The slurries were rolled into 100 μm thick freestanding electrode films with a rolling mill, and a 13 mm diameter hole punch subsequently excised identical circular electrodes out of the film sheet. Electrochemical cells were assembled inside an Ar-filled glove box in symmetrical, two-electrode configurations. Cells used L-shaped carbon-coated aluminum current collectors, and 2 layers of 3501 Celgard separator were inserted between the electrodes. The specific ionic liquids soaked the separator sheets prior to experiment in order to introduce the electrolyte to the electrodes.

Electrochemical measurements included three different techniques.[27] Electrochemical impedance spectroscopy (EIS) measurements collected real and imaginary impedance by oscillating voltage (10 mV amplitude) centered on 0.0 V vs. OCP with a dampening oscillation in the 200 kHz – 10 mHz frequency range. Cyclic voltammetry (CV) sweeps were carried out at varying sweep rates between 0.5 mV $s^{-1}$ and 1000 mV $s^{-1}$ in the 0 ↔ +2.5 V window (net potential difference between the two electrodes). Gravimetric capacitance ($C_{sp}$) was calculated according to the following equation:

$$C_{sp} = 2\int_{V_o}^{V_f} \frac{I}{\frac{dV}{dt} m_E V_W} dV \qquad [1]$$

The equation uses $V_0$ as the initial potential (fixed at zero) and $V_f$ as the vertex potentials; $m_E$ as the mass of a single electrode; $V_w$ is the electrochemical potential window (2.5 V); and $\frac{dV}{dt}$ is the sweep rate.[27] Square wave chronoamperometry (SWC) applied instantaneous 1.0 V, 2.0 V, and 2.5 V potential differences across the cell. SWC recorded time-resolved current during 60 minutes of steady-state potential conditions and subsequently derived total accumulated charge for each measurement.

***Classical density functional theory (cDFT) calculations.***—The computational approach adopted a coarse-grained model that represented imidazoles with positively charged spheres that were tangentially connected to a chain of neutral spheres. Therefore, each neutral sphere amounted to a propyl (3-carbon) group. Single negatively charged spheres represented the $TFSI^-$ anions. Prior to the analyses, we estimated the sphere dimensions and densities of ionic liquids from the work done by Ye and Shreeve.[28] A slit pore model with a fixed wall surface potential represented pores and exhibited dimensions that matched the porosity of the experimental OMC material. The theoretical details and a schematic (Fig. S1) of this model is given in Supplementary Information.

***Quasi-elastic neutron scattering (QENS).***—OMC powders, synthesized as reported,[22] were infiltrated with the three electrolytes according to the previously reported procedure.[29] C3mimTFSI and C12mimTFSI fully filled the volume of OMC pores of specific powder quantities (the SI section on the QENS measurements that describes the pore filling method). Small angle neutron scattering (SANS) profiles (Fig. S3) of empty and the ionic liquids (C3mimTFSI and C12mimTFSI) filled OMC show that the ionic liquids are present inside the pores (see SI for SANS details).QENS studies were carried out on the cold neutron multi-chopper spectrometer (LET)[30] in Oxfordshire, UK that was operated in repetition rate multiplication mode.[31] These capabilities of the LET allow data collection at several incident wavelengths to probe the dynamics which span different time scales. We performed an experiment at the LET using four incident energies (560, 860, 1340 and 2500 μeV), which yielded the data sets with the following energy resolutions (full width at half-maximum, FWHM): 3.95, 8.43, 18.2 and 44.0 μeV, with the corresponding momentum transfer (Q-coverage) of [0.3−0.7], [0.3−1.0], [0.3−1.4] and [0.3−1.85] $Å^{-1}$. QENS spectra were measured at 300 K from [$C_n$mim$^+$][$TFSI^-$] with a carbon chain length n = 3 and 12 confined in OMC of average pore size of 7.3 nm. Sample-specific resolution spectra were measured at 5 K. Desired sample temperatures was maintained using closed cycle refrigerator (CCR). Data were reduced and analyzed by Mantid[32] and DAVE[33] software, respectively.

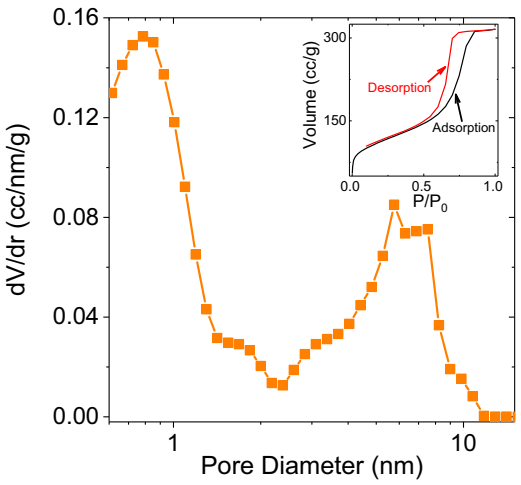


**Figure 1.** Semilogarithmic plot of ore size distribution for the ordered mesoporous carbon (OMC) studied in this work. Inset includes the nitrogen sorption/desorption isotherms.

## Results and Discussion

The pore size distribution for ordered mesoporous carbon is shown in Figure 1. Its isotherm (shown in the inset) exhibited typical Type IV behavior with pronounced hysteresis, suggesting a significant contribution of mesopores to the total porosity.[34] Nitrogen adsorption analysis indicated that the specific surface area (SSA) of the carbon material was 390 $m^2$ $g^{-1}$, and the total pore volume was 0.47 $cm^3$ $g^{-1}$. While the material exhibited some micropores (0.79 nm was the most predominant diameter), this narrow pore range contributed less than 25% of the cumulative accessible surface. The pore structure was mostly comprised of mesopores.

The electrode material's mesopores (2.0 nm−10.0 nm predominant pore diameter range for OMC, 7.3 nm most commonly occurring slit width) could accommodate all ion species of both electrolytes without limiting their individual translational and rotational motion. The dimension of the C3mim$^+$ cation and $TFSI^-$ anion were remarkably similar (respectively, 1.03 nm and 1.10 nm lengths; 0.65 nm and 0.5 nm widths; and 0.14 $nm^3$ and 0.15 $nm^3$ molecular volumes). Furthermore, all three ions were able to rotate freely among two axes in the micropores. However, the C12mim$^+$ cation's larger size (2.18 nm width and 0.29 $nm^3$ volume) significantly inhibited its ability to rotate along all three axes in the 0.78 nm wide micropores. Subsequently, for

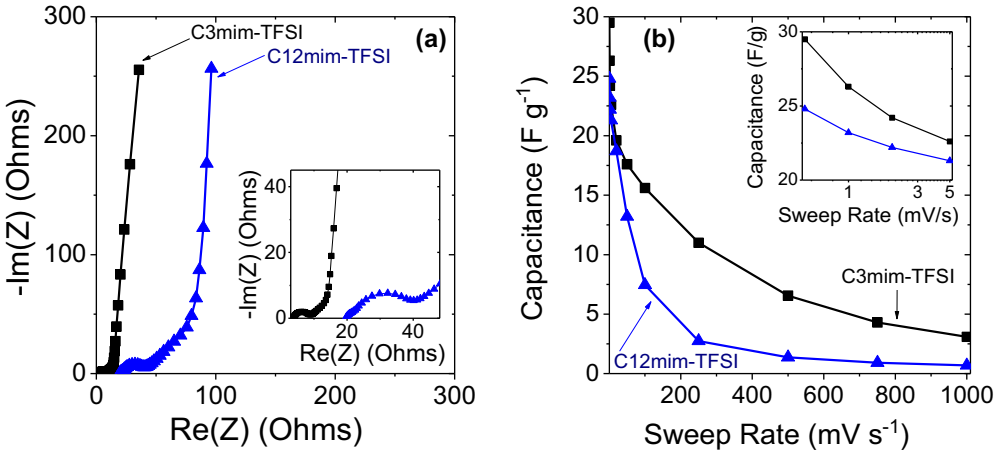


**Figure 2.** (a) The Nyquist plot compares the electrochemical impedance of C3mimTFSI and C12mimTFSI in ordered mesoporous carbon. Inset zooms in the high-frequency region. (b) Plot of rate handling comparison for the two electrolytes as from cyclic voltammetry scans in the 0.2−1000 mV/s sweep range.

C12mimTFSI, ion sieving limitations and resulting impedance were expected to negatively impact electrosorption rates and charge accumulation capabilities into smaller pores. Although the mesopores constituted a greater fraction of the entire pore architecture, and thus accounted for most of the observed charge storage behavior and electrolyte dynamics, "electrowetting" of smaller pores became an important factor that affected experimental supercapacitor performance in higher-voltage regimes.

Electrochemical tests of the two electrolytes showed distinct capacitance and electrodynamic differences between the two electrolytes in this micro- and meso-porous carbon system. From a mobility perspective, the Nyquist plot in Figure 2a shows the dynamics of C3mimTFSI and C12mimTFSI in OMC pores under a rapidly fluctuating potential. As expected, the C3mimTFSI electrolyte exhibits greater ionic mobility and lower ionic impedance for the entire frequency range. The equivalent series resistance (ESR), as determined by Re(Z) at -Im(Z) = 0,[35] was 3.7 Ω for C3mimTFSI and 19.7 Ω for C12mimTFSI. The charge transfer resistance (semi-circular region) was, similarly, much larger for the electrolyte with a longer chain length for the cation. The "knee frequency" time constant for C3mimTFSI was 4.7 s while that for C12mimTFSI is 28.8 s. Even low-frequency behavior featured relatively greater impedance for the C12mimTFSI electrolyte: its impedance angle (Phase (Z)) was −69° at 10 mHz, whereas C3mimTFSI was much more capacitive at the same frequency (Phase (Z) = −82°). The impedance behavior suggests that the large alkyl chain on the $C12mim^+$ cation of C12mimTFSI imposed noticeable mobility limitations on both short-range, rapid interactions and long-range, extended time-scale processes. In the case of the former (rapid co-ion/counterion exchange at electrode/electrolyte interfaces during high-frequency voltage fluctuations), the relative sluggish process and slow motion of the large cations with respect to the anions imposes detrimental effects on current flow through electrodes of C12mimTFSI system. These effects translate into higher equivalent series and charge transfer resistance values observed for the electrolyte with larger chain lengths on the cation. Furthermore, at longer time scales (that account for long-range diffusion of ions through the bulk electrode across the entire ultracapacitor), relative mobilities of larger $C12mim^+$ cations limit the resulting charge/discharge rates. Consequently, impedance-induced ionic resistance precludes the entire C12mimTFSI system from behaving as an ideal capacitor at near-static states. The impedance results for these charge storage systems, which used the same anions for both electrolytes, reinforced the concept that co-ion and counterion mobilities are intertwined.

Results of CV capacitance calculations over the entire 0.5−1000 mV $s^{-1}$ sweep range are shown in Figure 2b. In behavior that parallels the EIS results, C3mimTFSI showcased higher capacitance than C12mimTFSI throughout the entire scan rate range. As expected, C3mimTFSI benefited from the enhanced electrolyte dynamics and retained more capacitance at higher charge/discharge rates (≥20 mV $s^{-1}$). However, these differences were not significant at low sweep rates (≤ 5 mV $s^{-1}$). In fact, in that range, C3mimTFSI's rate handling decayed by 23%, while C12mimTFSI decayed by only 14%. Conversely, in the 20 mV/s–1000 mV/s, C3mimTFSI experiences a capacitance decay of 84%, while C12mimTFSI's capacitance decays by over 96% over the same sweep range.

Specific voltammograms at different sweep rates provide more insight into this observation. Figure 3a shows the CV sweeps at 2 mV $s^{-1}$. At this low charge/discharge rate, both data sets maintained relatively similar rectangular shapes, and ionic impedance did not drastically interfere with electrosorption at low voltages. The low-voltage plots segment shows greater rates of charge accumulation for C12mimTFSI up to 1.0 V. However, past that threshold, capacitance of C3mimTFSI increased, whereas capacitance of C12mimTFSI plateaued. During the discharge process, the C3mimTFSI system showed some evidence of ion saturation (a "butterfly" shape) at low voltages;[36] this behavior was absent for the electrolyte with the larger cation chain length. At higher rates (50 mV $s^{-1}$, Figure 3b), this charge saturation behavior was still present for C3mimTFSI. However, this rapid charge/discharge rate enhanced the ionic resistance and induced significant deviations of the C12mimTFSI system from its ideal rectangular CV curve. These takeaways suggest that, while both electrolytes electrosorb into mesopores with relative similar ease, narrower micropores (Fig. 1) exclude C12mimTFSI and limit its capacitance. Recent results in a bimodal porous carbon system exhibited similar findings.[17] The overall trends of cyclic voltammogram results paralleled those of impedance measurement results: lower mobility of $C12mim^+$ increases its resistance and, as compared to $C3mim^+$, lowers its capacitance and rate handling ability. The relative time scales affect the extent to which these observations parallel each other. At low impedance oscillation frequencies (and corresponding low sweep rates), the phase angle measurements and capacitance values deviate only slightly. However, the fivefold higher series resistance at high oscillation rates parallels the significant capacitance decay of the C12mimTFSI system.

Square wave chronoamperometry shown in Figure 3c delves more deeply into the processes that occur at each voltage. Steady-state charging up to 1.0 V results in the same charge accumulation for both electrolytes. This finding parallels the results from slow sweep rates shown for CVs. However, at 2.0 V, C3mimTFSI collects a significantly greater amount of charge than C12mimTFSI (Figure 3d). This behavior, likewise, corroborates the cyclic voltammogram sweeps in the higher voltage region. The dynamic and static electrochemical tests suggest that the alkyl chain length influences ion saturation and filling of pores,[37] and that this process primarily depends on the specific applied potential of the system.[38] Furthermore, since the pore structure

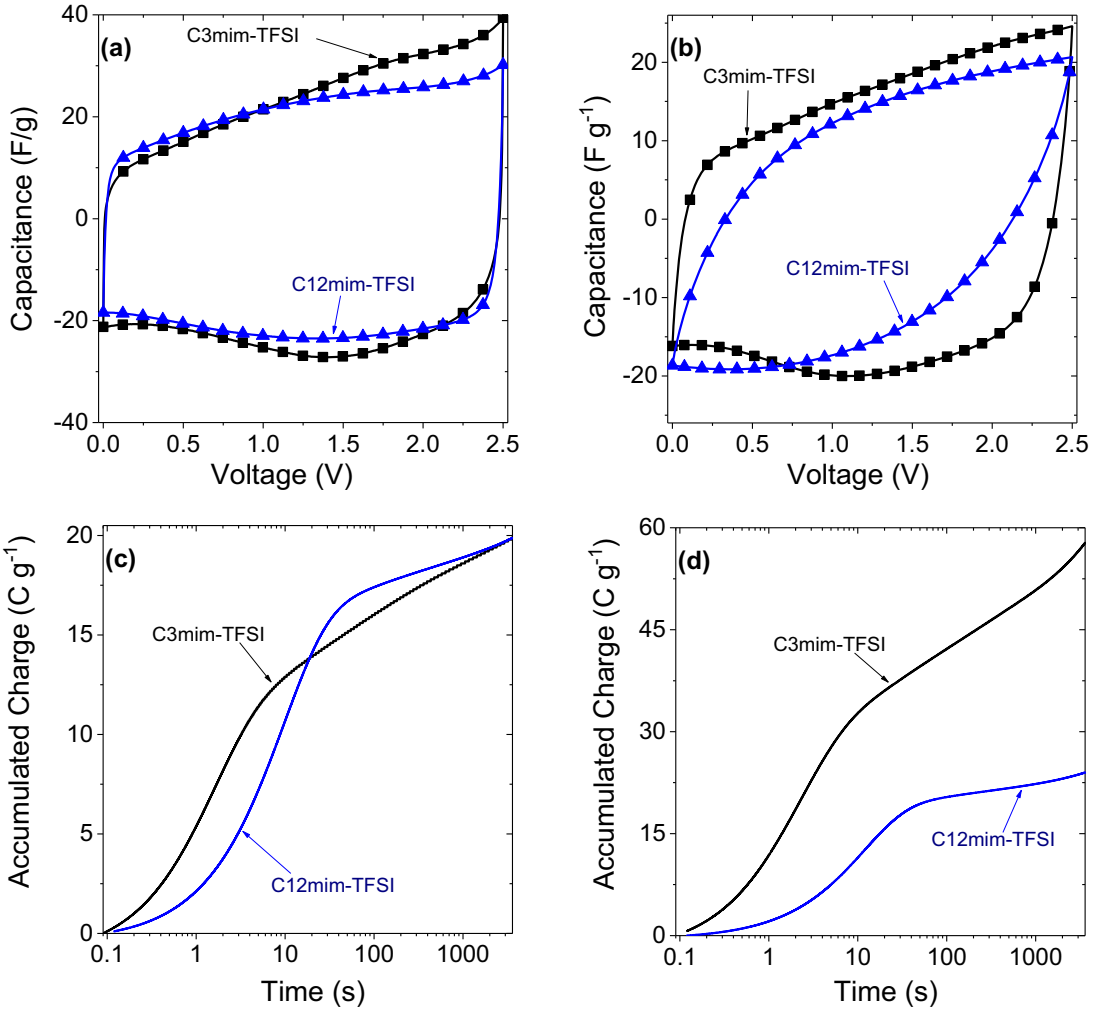


**Figure 3.** (A) Cyclic voltammetry in the 0–2.5 V window at 2 mV/s rate. (B) Cyclic voltammetry at a 50 mV/s sweep rate. (C) Square-wave chronoamperometry comparison of charging of C3mimTFSI and C12mimTFSI up to 1.0 V. (D) Square-wave step charging up to 2.0 V. C, D are semilogarithmic plots.

includes micropores and mesopores, "electrowetting" of small pores may only occur under higher applied potentials.[39] Since $C12mim^+$ has greater dimensional limitations than $C3mim^+$, only the latter may take advantage of micropores and increase capacitance at higher voltages.

From the aforementioned experiments, we note distinct behaviors that stem from the electrode material's dominant micropore region and mesopore region. From square wave chronoamperometry measurements, we find that capacitance capability of C12mimTFSI underperforms that of C3mimTFSI by ∼16% at a high voltage. However, in-depth voltage-dependent analysis and data refinement show that C3mimTFSI and C12mimTFSI mirror each other's performance until the potential exceeds −1.0 V vs. OCP. Beyond this threshold, the capacitance for C12mimTFSI changes only slightly while C3mimTFSI's charge accumulation continues to rise with voltage. Therefore, we conclude that there must be a substantial change in the fundamental charging and ion arrangement under applied voltages greater than −1.0 V vs. OCP that leads to this trend.

To complement electrochemical experimental results, we performed cDFT calculations to provide insights into the structure and properties of the EDL for this system. We approximated the mesopore pore size to be equal to 7.6 nm for subsequent calculations. For the cDFT calculations, we chose to examine the negative electrode only as we found that the positive electrode showed only minor changes with cation (not shown here). Here, applied potential refers to the potential on an individual electrode and the difference between the positive and negative electrode is the cell voltage. The computed capacitance versus applied potential (Figure 4) for the studied system shows that the capacitance is lower for C12mimTFSI relative to C3mimTFSI and, at −1.0 V, the capacitance is lower by 10%. The density profiles in Figure 5 provide further insight into the reduced capacitance of C12mimTFSI relative to C3mimTFSI. Although the number density

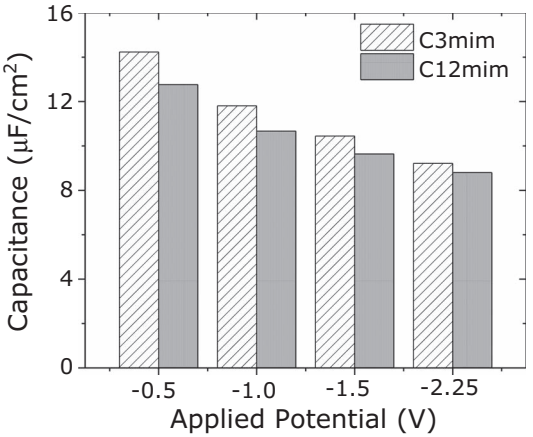


**Figure 4.** Variation of cDFT capacitance with applied potential for the ionic liquids C3mimTFSI and C12mimTFSI confined in a mesopore (7.6 nm).

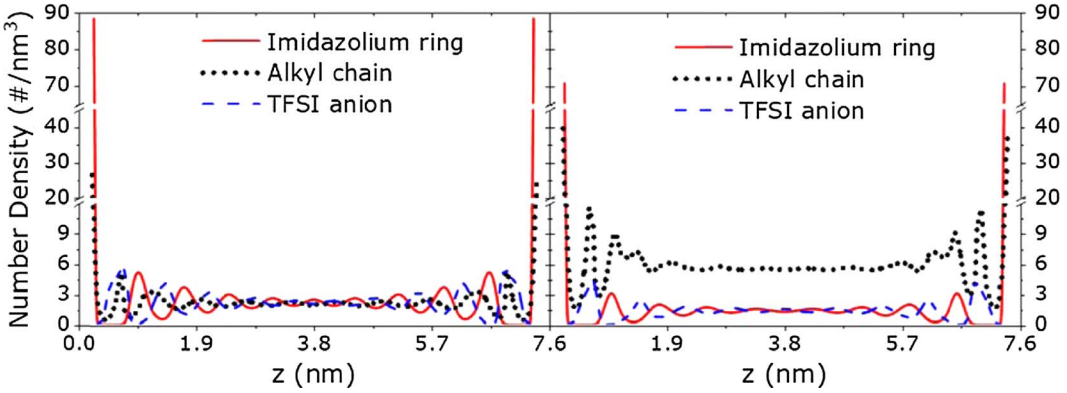


**Figure 5.** The number density profiles for C3mimTFSI (left panel) and C12mimTFSI (right panel) in a mesopore (7.6 nm) with an applied surface potential of −1.0 V.

profiles between the two ionic liquids are similar, there is a noticeable decrease in the contact density of the cation and the oscillation of the EDL structure when the alkyl chain length is increased. This results in a less packed EDL structure and provides more freedom for the alkyl chain which tends to spread away from the wall. As a result, there is a lower net charge accumulation in the pore that leads to a lower capacitance. It should be noted that in the smaller mesopores, the ions tend to occupy the space only near the wall with the neutral chain spreading across the pore providing freedom for the motion of the chains in the center of the pore. This is demonstrated by the density profiles (Fig. S2) of the ions in 2.6 nm pores.

Insight provided by the mesopore calculation, however, fails to provide a reason for why the electrochemical results show a potential at which the $C12mim^+$ charge accumulation is greatly hindered. To understand this, we focused on the material's microporous region by performing cDFT calculations with a pore size of 0.70 nm. We found that this region correctly matches the observed capacitance plateau for C12mimTFSI (shown in Figure 6a). To understand this plateau, we plot the number of ions with respect to the applied potential in Figures 6b. Here it becomes clear that the micropore is filled with only cations at −1.0 V, and further negative increase in applied potential results in a smaller increase in cations relative to when there were anions present. The lower negative potential threshold for anion depletion for C12mimTFSI compared to C3mimTFSI can be explained by the alkyl chain effectively displacing the anions from the micropore. As a result, the charge accumulation is much lower for C12mimTFSI than for C3mimTFSI past this potential threshold and explains the electrochemical results.

We employed QENS technique to study the microscopic dynamics of C3mimTFSI and C12mimTFSI confined in OMC. QENS has been a technique of choice to probe the dynamics of confined fluids.[40–42] Since hydrogen has very high neutron incoherent scattering cross-section,[43] the hydrogen atoms present in the cation of the RTILs dominates the QENS signal. Dynamic susceptibility (Fig. S4) derived from QENS spectra reveals a localized, non-Debye-like dynamics in both systems. Therefore, a Cole-Cole distribution function[44] was used to analyze the QENS data (see SI for details). Representative spectra together with a Cole-Cole model fits are presented in Figure S5 in Supplementary Information. Figures 7a and 7b shows a Q dependence of the HWHM of the QENS signal for both C3mimTFSI and C12mimTFSI measured with different incident neutron energies used. The values of HWHM tend to be somewhat higher for C12mimTFSI (Fig. 7b) compared to those for C3mimTFSI (Fig. 7a). This is unexpected, because higher HWHM values obtained for C12mimTFSI confined in OMC suggest higher detected mobility of $C12mim^+$ ions, that are larger than $C3mim^+$ ions, which would be counterintuitive. It has already been shown that the dynamics of cations becomes significantly reduced when the size of the cations increases.[45] Therefore, $C12mim^+$ is expected to exhibit slower mobility. However, we note that the dependence of the HWHM in Figures 7a and 7b is not quadratic with Q, as one would expect for translational diffusion of ions, thus suggesting that we are not probing the diffusivity of the entire cations. Instead, the

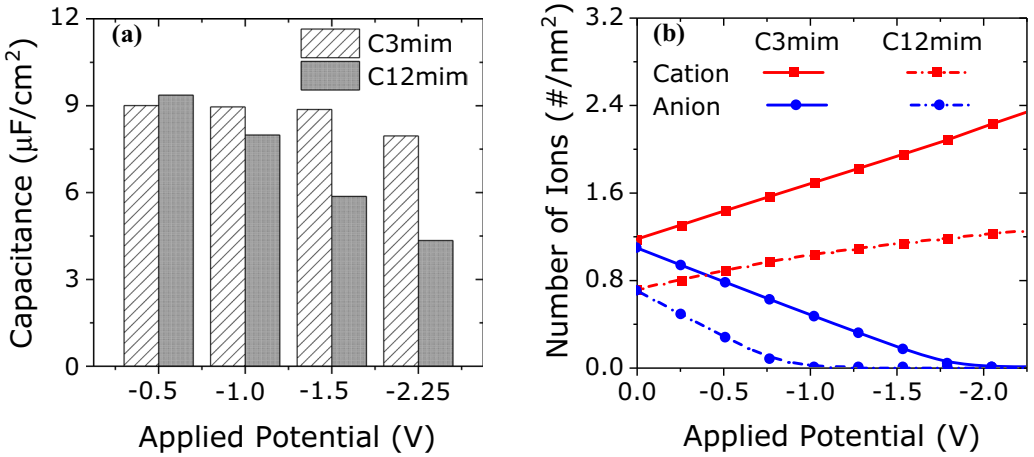


**Figure 6.** The capacitance at different applied potentials (a) and the number of ions present at different applied potentials (b) for C3mimTFSI and C12mimTFSI in a micropore (0.7 nm).

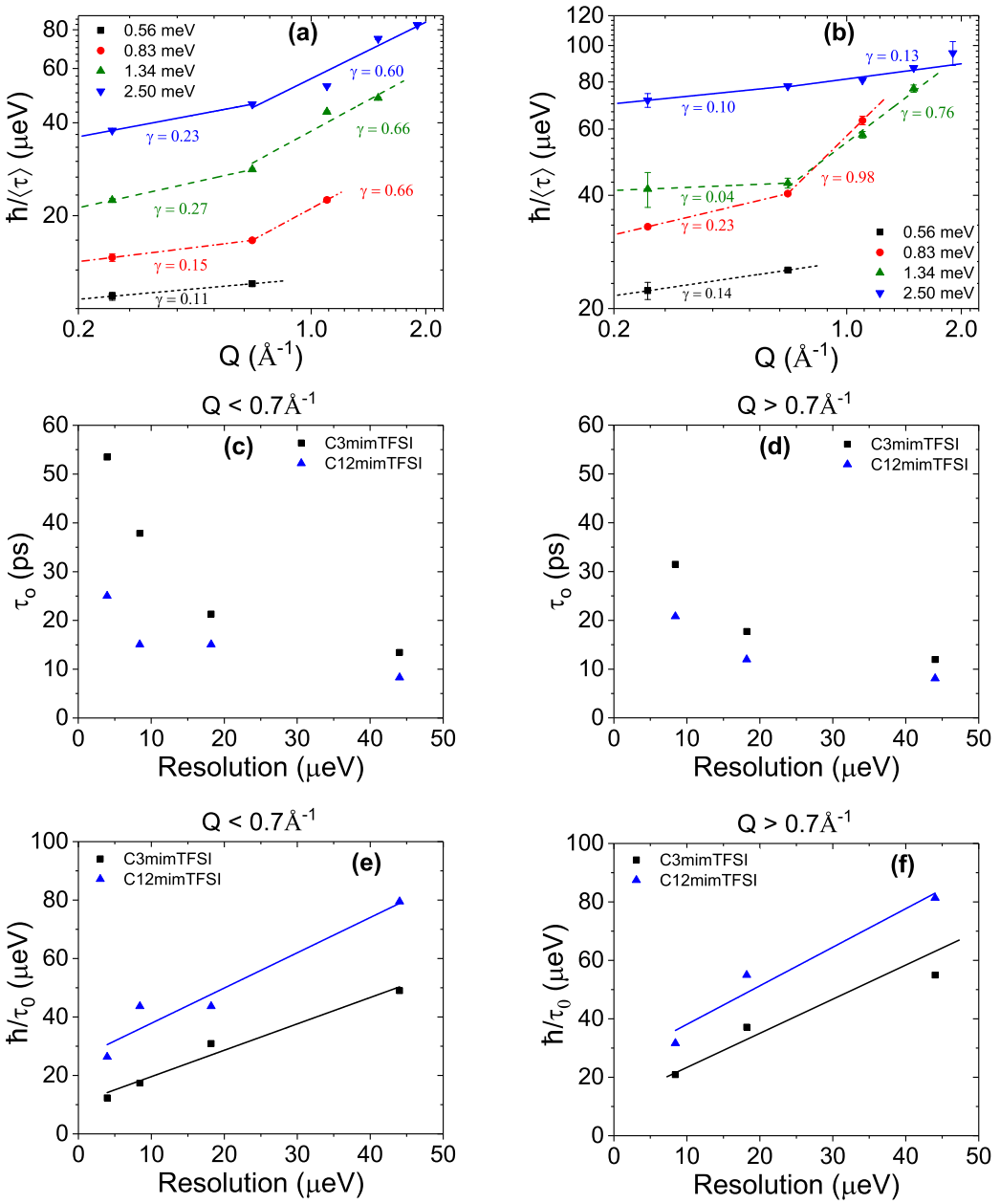


**Figure 7.** Q dependence of the QENS signal HWHM (a) C3mimTFSI (b) C12mimTFSI, showing a crossover at ~Q = 0.7 Å$^{-1}$, where γ is the corresponding slope of the lines. Calculated structural relaxation time, $\tau_0$, in the two Q regimes (c) and (d) with the corresponding Q-averaged QENS broadening (e) and (f). The values are plotted as a function of the instrument resolutions associated with the varied incident neutron energies used in the QENS measurement.

QENS measurement is exploring the local mobility of the alkyl chains of the cations. This is further evidenced by the low values of the power law exponent (see SI for scaling of structural relaxation time).

Overall, there is not a strong dependence of ⟨τ⟩ (which is inversely proportional to the HWHM) with Q. However, a clear crossover is present at Q = 0.7 Å$^{-1}$, which is equivalent to a length scale of ~ 9 Å. Because this length scale approximately corresponds to the size of the OMC micropores as presented in Figure 1, it would be tempting to associate the data above and below the crossover with the cation dynamics in the micro- and meso-pores, respectively. However, it is unlikely that the cation dynamics in the mesopores could be more spatially restricted, with a weaker Q-dependence than that in the micropores. Instead, the mobility probed in the QENS experiment is associated with the side chains of the cations, exploring the localized volume near the cation. The localized motions of this type are known to exhibit a crossover in the Q-dependence of their HWHM at the length scale corresponding to the characteristic size of the effective localized volume inside which the motion takes place.[43]

This higher value of HWHM from C12mimTFSI also implies that, when the length of the side chain attached to the imidazole ring increases, its mobility decouples from the mobility of the ring. The long-range diffusivity of the cation, as whole, decreases with the cation size, yet the longer chains exhibit greater localized mobility. This is consistent with the density spikes observed in cDFT calculation for $C12mim^+$ away from the pore walls in Figure 5, where the chain is less affected by the interaction between the ions with the wall of the pores. In C3mimTFSI, the chain is shorter, and its mobility couples with that of the imidazole ring, resulting in the relatively lower chain's mobility compared to the chain in C12mimTFSI.

While the data in Figure 7 provide information on the Q-dependence and, thus, the geometry effects on the cation motions, the quantitative information on the time scale of the cation motions

needs to be extracted from the parameter $\tau_0$, the structural relaxation time, obtained from the $\langle\tau\rangle = \tau_0 Q^{-\gamma}$ relationship. In Figures 7c–7f, this parameter is plotted for C3mimTFSI and C12mimTFSI as a function of the instrument resolution that varies with the incident neutron energy. In agreement with the data in Figures 7a–7b, $C3mim^+$ ions exhibit relatively longer structural relaxation times, that is, slower dynamics, compared to $C12mim^+$ ions (Figures 7c–7d). Shorter structural relaxation time for the larger $C12mim^+$ ions is an indication of the dynamic decoupling between the main ring and the side chain, similar to the dynamic decoupling observed in an ionic liquid with octyl side chain.[46] While the longer chains of the $C12mim^+$ exhibit enhanced localized mobility, the electrochemical performance is directly influenced by the mobility of cations as a whole, and the larger size of $C12mim^+$ results in a smaller capacitance compared to that of $C3mim^+$.

The inverse of the structural relaxation time, corresponding to the QENS broadening effectively averaged over all Q values, shows approximately linear dependence with the instrument resolution (Figures 7e–7f). This again suggests that the motions probed in the current QENS measurement are not related to the long-range translational diffusion of cations as a whole, which is characterized by a well-defined diffusivity value and is thus expected to be resolution-independent. Instead, the QENS measurements probe a broad range of motions associated with the localized mobility of the alkyl chains of the cations, as already evidenced by the resolution-dependent shift of the low-energy peak in the susceptibility plots in Figure S4. The susceptibility plots in Figure S4 are essentially the model-independent raw data demonstrating that the measured characteristic relaxation time is indeed resolution-dependent. Depending on the energy resolution, the broadly distributed in time chain motions are weighed differently, thus giving rise to different average relaxation times. Decoupling of the chain from the imidazolium ring may help ion exchange at the electrode/electrolyte interface and compensate somewhat for its larger size, but that effect is hard to measure at this time and will need to be investigated in the future.

## Summary

A combination of electrochemical measurements with QENS and cDFT allowed identification of the fundamental reasons behind differences in dynamics, electrosorption rates, and charge accumulation densities that occur when ionic liquid electrolytes with different cation alkyl chains are confined inside mesoporous carbon. Our combinational approach probed the influence of the electrolyte structure (alkyl chain length) on the charging behavior, arrangement, and dynamics of ions, and the corresponding changes in energy and power densities of supercapacitors. Although the takeaway with respect to the dynamics – $C3mim^+$ is smaller and likely exhibits greater mobility than $C12mim^+$ – appears intuitive, neutron scattering allowed us to probe the mobilities of individual components and added greater depth to the underlying mechanisms that ordinary electrochemistry measurements cannot capture. Specifically, our approach suggested that sufficiently long alkyl chains on cations begin to undulate and move independently of the imidazolium ring. This observation was further supported by the high-density peaks, observed away from the pore walls, for the ionic liquid cation bearing longer alkyl chain, i.e., C12mimTFSI. Such behavior has never been observed before for confined electrolytes. This type of dynamic decoupling may benefit ion exchange phenomena at fluid-solid interface of energy storages devices and demands more rigorous research in the future. Furthermore, while larger ion size was also expected to reduce overall capacitance, our computational approach found the reasons why this decline is contingent on the specific applied voltage. In particular, past a critical −1.00 V threshold, cation concentration of the C12mimTFSI system becomes depleted in pores, and capacitance of the larger ion system becomes lower than that of the C3mimTFSI by 16%. These complex mechanisms, which cannot be captured by traditional testing and characterization techniques, are essential for future electrode and electrolyte design.

## Acknowledgments

This work was supported as part of the Fluid Interface Reactions, Structures and Transport (FIRST) Center, an Energy Frontier Research Center funded by the U.S. Department of Energy, Office of Science, Office of Basic Energy Sciences. Work at ORNL's Spallation Neutron Source and High Flux Isotope Reactor was sponsored by the Scientific User Facilities Division, Office of Basic Energy Sciences, U.S. Department of Energy. Oak Ridge National Laboratory is managed by UT-Battelle, LLC, for U.S. DOE under Contract No. DEAC05-00OR22725. Experiments at the ISIS Neutron and Muon Source were supported by a beamtime allocation (RB1520027) from the Science and Technology Facilities Council. This work is also supported by the National Science Foundation Graduate Research Fellowship under grant No. DGE-1326120.

## ORCID

Naresh C. Osti https://orcid.org/0000-0002-0213-2299
Eugene Mamontov https://orcid.org/0000-0002-5684-2675

## References

1. J. Kalhoff, G. G. Eshetu, D. Bresser, and S. Passerini, *ChemSusChem*, **8**(13), 2154 (2015).
2. U. A. Rana, M. Forsyth, D. R. MacFarlane, and J. M. Pringle, *Electrochimica Acta*, **84**, 213 (2012).
3. D. R. Macfarlane, M. Forsyth, P. C. Howlett, J. M. Pringle, J. Sun, G. Annat, W. Neil, and E. I. Izgorodina, *Accounts of Chemical Research*, **40**(11), 1165 (2007).
4. D. R. MacFarlane, N. Tachikawa, M. Forsyth, J. M. Pringle, P. C. Howlett, G. D. Elliott, J. H. Davis, M. Watanabe, P. Simon, and C. A. Angell, *Energy & Environmental Science*, **7**(1), 232 (2014).
5. M. Galinski, A. Lewandowski, and I. Stepniak, *Electrochimica Acta*, **51**(26), 5567 (2006).
6. M. Watanabe, M. L. Thomas, S. G. Zhang, K. Ueno, T. Yasuda, and K. Dokko, *Chemical Reviews*, **117**(10), 7190 (2017).
7. J. Vatamanu, Z. Z. Hu, D. Bedrov, C. Perez, and Y. Gogotsi, *Journal of Physical Chemistry Letters*, **4**(17), 2829 (2013).
8. T. Chen and L. M. Dai, *Materials Today*, **16**(7−8), 272 (2013).
9. G. P. Wang, L. Zhang, and J. J. Zhang, *Chemical Society Reviews*, **41**(2), 797 (2012).
10. P. Simon and Y. Gogotsi, *Nature Materials*, **7**(11), 845 (2008).
11. Q. W. Yang, Z. Q. Zhang, X. G. Sun, Y. S. Hu, H. B. Xing, and S. Dai, *Chemical Society Reviews*, **47**(6), 2020 (2018).
12. M. Beidaghi and Y. Gogotsi, *Energy & Environmental Science*, **7**(3), 867 (2014).
13. V. L. Martins and R. M. Torresi, *Current Opinion in Electrochemistry*, **9**, 26 (2018).
14. A. Vlad and A. Balducci, *Nature Materials*, **16**(2), 161 (2017).
15. X. L. Chen, R. Paul, and L. M. Dai, *National Science Review*, **4**(3), 453 (2017).
16. R. Lin, P. Huang, J. Segalini, C. Largeot, P. L. Taberna, J. Chmiola, Y. Gogotsi, and P. Simon, *Electrochimica Acta*, **54**(27), 7025 (2009).
17. B. Dyatkin, N. C. Osti, Y. Zhang, H.-W. Wang, E. Mamontov, W. T. Heller, P. Zhang, G. Rother, P. T. Cummings, D. J. Wesolowski, and Y. Gogotsi, *Carbon*, **129**, 104 (2018).
18. N. Jackel, P. Simon, Y. Gogotsi, and V. Presser, *ACS Energy Letters*, **1**(6), 1262 (2016).
19. Y. He, R. Qiao, J. Vatamanu, O. Borodin, D. Bedrov, J. Huang, and B. G. Sumpter, *J Physical Chemistry Letters*, **7**(1), 36 (2016).
20. R. Futamura, T. Iiyama, Y. Takasaki, Y. Gogotsi, M. J. Biggs, M. Salanne, J. Segalini, P. Simon, and K. Kaneko, *Nature Materials*, **16**(12), 1225 (2017).
21. E. Eustache, C. Douard, A. Demortiere, V. De Andrade, M. Brachet, J. Le Bideau, T. Brousse, and C. Lethien, *Advanced Materials Technologies*, **2**(10), 17001126 (2017).
22. C. D. Liang and S. Dai, *Journal of the American Chemical Society*, **128**(16), 5316 (2006).
23. S. Brunauer, P. H. Emmett, and E. Teller, *Journal of the American Chemical Society*, **60**(2), 309 (1938).
24. G. Y. Gor, M. Thommes, K. A. Cychosz, and A. V. Neimark, *Carbon*, **50**(4), 1583 (2012).
25. B. Dyatkin, V. Presser, M. Heon, M. R. Lukatskaya, M. Beidaghi, and Y. Gogotsi, *ChemSusChem*, **6**(12), 2269 (2013).
26. C. R. Perez, S. H. Yeon, J. Segalini, V. Presser, P. L. Taberna, P. Simon, and Y. Gogotsi, *Advanced Functional Materials*, **23**(8), 1081 (2013).
27. M. D. Stoller and R. S. Ruoff, *Energy & Environmental Science*, **3**, 1294 (2010).
28. C. F. Ye and J. M. Shreeve, *Journal of Physical Chemistry A*, **111**(8), 1456 (2007).
29. B. Dyatkin, E. Mamontov, K. M. Cook, and Y. Gogotsi, *Progress in Natural Science-Materials International*, **25**(6), 631 (2015).
30. R. I. Bewley, J. W. Taylor, and S. M. Bennington, *Nuclear Instruments & Methods in Physics Research Section a-Accelerators Spectrometers Detectors and Associated Equipment*, **637**(1), 128 (2011).
31. F. Mezei, *Physica B-Condensed Matter*, **385–86**, 995 (2006).
32. O. Arnold, J. C. Bilheux, J. M. Borreguero, A. Buts, S. I. Campbell, L. Chapon, M. Doucet, N. Draper, R. F. Leal, M. A. Gigg, V. E. Lynch, A. Markvardsen,

D. J. Mikkelson, R. L. Mikkelson, R. Miller, K. Palmen, P. Parker, G. Passos, T. G. Perring, P. F. Peterson, S. Ren, M. A. Reuter, A. T. Savici, J. W. Taylor, R. J. Taylor, R. Tolchenoy, W. Zhou, and J. Zikoysky, *Nuclear Instruments & Methods in Physics Research Section a-Accelerators Spectrometers Detectors and Associated Equipment*, **764**, 156 (2014).
33. R. T. Azuah, L. R. Kneller, Y. M. Qiu, P. L. W. Tregenna-Piggott, C. M. Brown, J. R. D. Copley, and R. M. Dimeo, *Journal of Research of the National Institute of Standards and Technology*, **114**(6), 341 (2009).
34. S. Lowell and J. E. Shields, *Powder surface area and porosity*, (Springer Science & Business Media, **2** (2013).
35. J. Segalini, B. Daffos, P. L. Taberna, Y. Gogotsi, and P. Simon, *Electrochimica Acta*, **55**(25), 7489 (2010).
36. O. Kimizuka, O. Tanaike, J. Yamashita, T. Hiraoka, D. N. Futaba, K. Hata, K. Machida, S. Suematsu, K. Tamamitsu, S. Saeki, Y. Yamada, and H. Hatori, *Carbon*, **46**(14), 1999 (2008).
37. R. Mysyk, E. Raymundo-Piñero, and F. Béguin, *Electrochemistry Communications*, **11**(3), 554 (2009).
38. S. Kondrat, P. Wu, R. Qiao, and A. A. Kornyshev, *Nature Materials*, **13**(4), 387 (2014).
39. S. Boukhalfa, D. Gordon, L. He, Y. B. Melnichenko, N. Nitta, A. Magasinski, and G. Yushin, *ACS Nano*, **8**(3), 2495 (2014).
40. N. C. Osti, A. Cote, E. Mamontov, A. Ramirez-Cuesta, D. J. Wesolowski, and S. O. Diallo, *Chemical Physics*, **465**, 1 (2016).
41. N. C. Osti, M. Naguib, A. Ostadhossein, Y. Xie, P. R. C. Kent, B. Dyatkin, G. Rother, W. T. Heller, A. C. T. van Duin, Y. Gogotsi, and E. Mamontov, *ACS Applied Materials & Interfaces*, **8**(14), 8859 (2016).
42. N. C. Osti, B. Dyatkin, M. W. Thompson, F. Tiet, P. F. Zhang, S. Dai, M. Tyagi, P. T. Cummings, Y. Gogotsi, D. J. Wesolowski, and E. Mamontov, *Physical Review Materials*, **1**(3), 035402 (2017).
43. M. Bee, *Quasielastic Neutron Scattering: Principles and Applications in Solid State Chemistry, Biology, and Materials Science*, (Adam Hilger, Bristol), (1998).
44. K. S. Cole and R. H. Cole, *The Journal of Chemical Physics*, **9**(4), 341 (1941).
45. B. Dyatkin, N. C. Osti, A. Gallegos, Y. Zhang, E. Mamontov, P. T. Cummings, J. Wu, and Y. Gogotsi, *Electrochimica Acta*, **283**, 882 (2018).
46. F. Ferdeghini, Q. Berrod, J. M. Zanotti, P. Judeinstein, V. G. Sakai, O. Czakkel, P. Fouquet, and D. Constantin, *Nanoscale*, **9**(5), 1901 (2017).